Estimating Loads Along Elastic Rods

Vincent A. Aloi Student Member, IEEE, D. Caleb Rucker Member, IEEE

Abstract — Mechanics-based models of thin elastic structures are prevalent in robotics research, both in soft/continuum robot modeling, and in robotic manipulation of strings, sutures, needles, and endoscopes. In all these applications, distributed loads along the device's length can affect its shape in space. Estimation of the distributed loading based on observation of the object's shape constitutes a classical mechanics inverse problem that would be useful in many applications, but this problem has received relatively little attention to date. In this paper, we propose methods to estimate distributed loads on an elastic rod using a large-deflection Cosserat-rod model and constrained nonlinear optimization. We perform experiments that illustrate the feasibility of using these methods to locate regions of high contact force along the rod, and to estimate magnitudes of the forces that are applied. Results show that overall force magnitudes and locations can be estimated with average error of 0.29 N (6.7% of average resultant magnitude) and 4 mm (2% of rod length) for complex double-bend shapes, and the shape approximation has near-zero error.

I. Introduction

In both medical robotics, soft/continuum robots and other slender elastic devices are increasingly being investigated. Many applications (e.g. flexible endoscopy, therapy with steerable needles, and surgical intervention with continuum robots) involve distributed forces between the device and the anatomy and/or point contact forces at unknown locations, and estimating these forces is key to increasing safety and effectiveness. The compliant nature of soft robots and continuum robots can potentially enable sensing of interaction forces using the deflection of the robot itself [1], [2]. This deflection-based estimation paradigm is especially attractive at small scales where dedicated force sensors are size prohibitive [3]. Many shape-sensing methods have been explored, based on imaging [3], [4], electromagnetic trackers [5], [6], and fiber-optic strain sensors [7], [8]. Sensing external end-effector forces based on sensed actuation load has been explored for multi-backbone [9] and parallel [10] continuum robots. In this paper, we focus on the deflection-based sensing problem, but estimation approaches that combine both shape data and actuation load data may provide additional advantages in the future. Beyond medical applications, the distributed force sensing problem is also important for robotics in general, e.g. in soft robot interactions with humans or in the manipulation of elastic objects like strings or sutures [11].

This material is based upon work supported by the National Science Foundation under IIS-1652588 (A CAREER Award). Any opinion, findings, and conclusions or recommendations expressed in this material are those of the authors and do not necessarily reflect the views of the National Science Foundation. V. A. Aloi and D. C. Rucker are with the Department of Mechanical, Aerospace, and Biomedical Engineering, University of Tennessee, Knoxville, TN (e-mail: valoi@utk.edu, caleb.rucker@utk.edu)

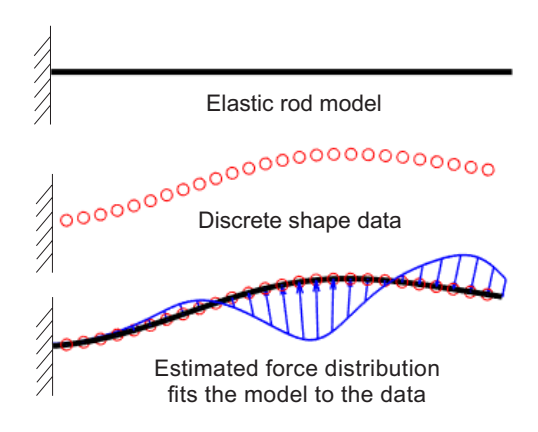


Fig. 1. Our approach to the distributed force estimation problem is to find a set of forces which minimizes the error between discrete shape data and a continuous rod model.

So far, most deflection-based force sensing efforts have focused on sensing a single force at the tip or end-effector [1]-[3], [8], [12], [13], while estimation of continuous force distributions along the length of the device remains a major challenge. Some research has explored sensing contacts along the shaft of a manipulator. Bajo [14], [15] designed a scheme to detect contact locations based on 6 DOF screw motions obtained through magnetic tracking, but did not estimate the forces themselves. Other soft robot modeling work has included inverse approaches to determine contact forces during simulation of soft robots in prescribed simulation environments [16]. Recently, a Kalman smoothing approach has been considered for the problem of estimating the full set of continuum robot state variables, potentially including discrete reaction forces at known locations [17], but the approach is not formulated to estimate general applied load distributions. For soft robot structures of general 3D shapes, [18] proposed a method that solves an finite-element inverse problem to estimate a number of point forces given the displacements of an equal number of feature points.

A. Approach and Contributions

In this paper, we use discrete shape data to estimate general force distributions on elastic rods by using a 3D large-deflection Cosserat rod model and a constrained optimization framework. We explore two variants of this approach based on different functional representations of the distributed load: (1) a truncated Fourier series, and (2) a set of discrete point forces with variable locations and magnitudes. Validation experiments with a spring steel rod subject to multiple loads along its length demonstrate the method's accuracy.

II. FORCE SENSING APPROACH

A. Constrained Optimization Framework

Given a set of N_p measured 3D positions \mathbf{d}_i ($i=1...N_p$) at nominal arc length positions s_i^* ordered and evenly spaced along a cantilevered elastic rod with known geometry and material properties, we propose to estimate the distributed force function $\mathbf{f}(s)$ along the arc length s of the rod by numerically solving the following constrained, nonlinear optimization problem based on the root-mean-squared error:

minimize
$$\sqrt{\frac{1}{N_p} \sum_{i=1}^{N_p} \|\mathbf{p}_i(\mathbf{x}) - \mathbf{d}_i\|_2^2}$$
 subject to
$$\mathbf{c}(\mathbf{x}) = \mathbf{0}$$
 (1)

where $\mathbf{p}_i(\mathbf{x})$ is the 3D position generated by the Cosserat rod model evaluated at arc length s_i . The vector of unknown parameters \mathbf{x} includes parameters which define the distributed load function $\mathbf{f}(s)$ (which we will detail later in the paper) in the Cosserat model, as well as unknown conditions at the base of the rod (the position $\mathbf{p}_0 \in \mathbb{R}^3$, the orientation $\mathbf{R}_0 \in \mathrm{SO}(3)$ (parameterized with Euler angles), the internal force vector $\mathbf{n}_0 \in \mathbb{R}^3$, and the internal moment vector $\mathbf{m}_0 \in \mathbb{R}^3$ at s=0). Note that for a cantilevered rod, we generally have a good initial estimate of the base position and orientation, but including them as unknown parameters in \mathbf{x} allows our optimization framework to compensate for uncertainty and "register" the model to the data as it simultaneously estimates the forces.

The arc lengths s_i at which the Cosserat model is evaluated should be close to the nominal arc length locations s_i^* of the data points. We use the optimization algorithm itself to identify the best model evaluation arc lengths (the ones eventually closest to the data points) by parameterizing each evaluation point (while keeping them ordered) as

$$s_i = s_i^* + \frac{h}{2}\sin\alpha_i$$

where h is the nominal spacing between the data points. The parameters α_i are then included in the unknown vector \mathbf{x} .

The constraint function c(x) includes the residual errors of any known boundary conditions. For the cantilevered rod with a free distal end that we experimentally investigate in this paper, this involves conditions on the internal force and moment at the distal end, as we detail in the next section. Under this constrained optimization formulation of the estimation problem, evaluation of the objective function only requires integrating an initial value problem defined by the Cosserat rod equations (as detailed in the next section). While we are using a standard Cosserat rod model as a test case in this paper, our basic framework is applicable to many continuum robot models which are commonly expressed as differential equations in arc length subject to various boundary conditions and constraints, e.g. [10], [19], [20]. We solve (1) numerically using the interior point algorithm as implemented in Matlab's fmincon(). While this paper

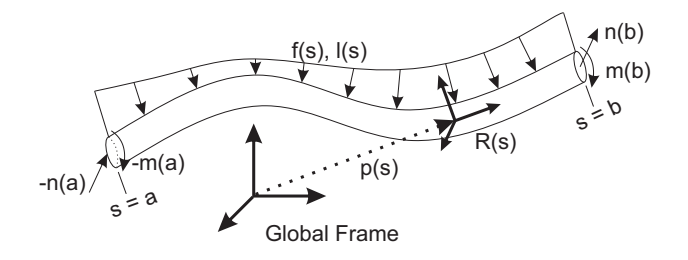


Fig. 2. The Cosserat equations are derived by performing a static balance over a section of rod. All the state variables are defined with respect to arc length and are referenced to an arbitrary global frame.

focuses on feasibility instead of computational speed, we note that Cosserat models can be integrated very efficiently [21], and the Jacobian of the objective function residuals with respect to \mathbf{x} can also be computed efficiently [22].

B. Cosserat Rod Model

Here we provide a brief review of the classic Cosserat rod equations and describe how to use them to evaluate the objective function defined in (1). The shape of a rod is described by the position of its centerline $\mathbf{p}(s) \in \mathbf{R}^3$, and a rotation matrix, $\mathbf{R}(s) \in \mathrm{SO}(3)$, representing its material orientation as a function of arc length s, as shown in figure 2. The derivatives of \mathbf{p} and \mathbf{R} with respect to s are defined by

$$\mathbf{p}' = \mathbf{R}\mathbf{v}$$

$$\mathbf{R}' = \mathbf{R}\widehat{\mathbf{u}},$$
(2)

where the kinematic variables $\mathbf{v}(s)$ and $\mathbf{u}(s)$ are the linear and angular rates of change of of a material attached transformation

$$\mathbf{g}(s) = \begin{bmatrix} \mathbf{R} & & \mathbf{p} \\ \mathbf{0}^\top & & 1 \end{bmatrix}$$

expressed in the local body-frame coordinates. The $\widehat{}$ operator, as defined in [23], maps \mathbb{R}^3 to $\mathfrak{so}(3)$ (the skew-symmetric matrices, the Lie algebra of the Lie group SO(3)).

Performing a static balance on a section of rod (Figure 2) and taking a derivative, we can describe the rates of change of the internal force vector $\mathbf{n}(s)$ and the internal moment vector $\mathbf{m}(s)$ with respect to arc length:

$$\mathbf{n}' = -\mathbf{f}$$

$$\mathbf{m}' = -\mathbf{p}' \times \mathbf{n} - \mathbf{l},$$
(3)

where ${\bf f}$ and ${\bf l}$ are vectors defining the external distributed force and distributed moment per unit arc length applied to the rod. In this paper we assume ${\bf l}={\bf 0}$, and we aim to estimate ${\bf f}(s)$

The internal force and moment vectors are related to \mathbf{v} and \mathbf{u} via a material constitutive law. Commonly, a linear law is used for static applications:

$$\mathbf{n} = \mathbf{R} \mathbf{K}_{se} (\mathbf{v} - \mathbf{v}^*), \quad \mathbf{m} = \mathbf{R} \mathbf{K}_{bt} (\mathbf{u} - \mathbf{u}^*)$$
 (4)

where \mathbf{v}^* and \mathbf{u}^* are appropriate kinematic variables of the rod in its stress free reference state ($\mathbf{u}^* = \mathbf{0}$ and $\mathbf{v}^* = [0\ 0\ 1]^\top$ for an initially straight rod), and $\mathbf{K}_{se} = \mathrm{diag}\left(GA, GA, EA\right)$ and $\mathbf{K}_{bt} = \mathrm{diag}\left(EI, EI, GJ\right)$ are stiffness matrices in terms of the rod's cross-sectional area A, Young's modulus E, shear modulus G, area moment of inertia I, and polar moment of inertia J. Combining Equations 2, 3, and 4, we have a system of differential equations that describe the evolution of \mathbf{p} , \mathbf{R} , \mathbf{n} , and \mathbf{m} with respect to s.

The parameter vector \mathbf{x} specifies a full set of conditions at s=0, and the distributed force function $\mathbf{f}(s)$. Thus any numerical integration routine for solving initial value problems can be used to obtain $\mathbf{p}(s)$ and evaluate the objective function in (1). In this paper, we use the adaptive step-size, 5^{th} order, Dormand-Prince algorithm as implemented by ode 45() in Matlab.

Similarly, $\mathbf{c}(\mathbf{x})$ can also be evaluated after numerical integration of the rod model given the initial conditions specified in \mathbf{x} . If there is a known point force \mathbf{F} and moment \mathbf{M} acting at the tip of a rod then the constraint function can be written as

$$\mathbf{c}(\mathbf{x}) = \begin{bmatrix} \mathbf{n}(L) - \mathbf{F} \\ \mathbf{m}(L) - \mathbf{M} \end{bmatrix}$$
 (5)

In this paper we explore the special case where the tip loads are zero (a cantilevered rod with a free end), but known tip loads could arise, for example, in robots actuated by cables with known tensions. Note that if zero tip loads are assumed when there is actually some unknown applied tip force, the solution to the optimization problem will simply yield an estimated distributed force which exhibits a concentrated peak near the tip which approximates the true tip load (as we show in our experiments).

C. Parameterization of Distributed Loads

We outline two possible ways to parameterize the unknown force distribution in the rod model. Each parameterization defines two functions $f_x^l(s)$ and $f_y^l(s)$ which specify the x and y components of the distributed force expressed in the local frame $\mathbf{R}(s)$. As mentioned above, we assume that the distributed force has zero component in the local axial (tangent) direction. The distributed load vector $\mathbf{f}(s)$ expressed in the global frame is then

$$\mathbf{f}(s) = \mathbf{R}(s) \begin{bmatrix} f_x^l(s) \\ f_y^l(s) \\ 0 \end{bmatrix}$$
 (6)

1) Fourier Series: First, we consider a truncated Fourier series approximation representation of the form

$$f_x^l(s) \approx a_{x0} + \sum_{k=1}^N a_{xk} \sin \frac{k\pi s}{L} + \sum_{k=1}^N b_{xk} \cos \frac{k\pi s}{L}$$

$$f_y^l(s) \approx a_{y0} + \sum_{k=1}^N a_{yk} \sin \frac{k\pi s}{L} + \sum_{k=1}^N b_{yk} \cos \frac{k\pi s}{L}$$
(7)

The number of Fourier terms N determines the resolution of the distributed force approximation, and the number of associated coefficients included in the unknown parameter

vector \mathbf{x} is 4N+2. One must use enough terms to adequately capture general distributed loads but not too many so that the algorithm remains efficient and is not overfitting the data. In our experimental analysis we used N=21 terms.

2) Sliding Dirac Deltas: While the Fourier series parameterization can accurately represent most smooth, slowly-varying (in arc length) distributed loads, a very large number of terms would be required to accurately estimate discontinuous loadings such as square waves or point loads. In these difficult cases, a Fourier approximation will tend to underestimate the peak magnitude of the distributed force, even if the shape data is well matched. This motivates the second distributed force representation that we explore in this paper, namely a collection of point loads distributed at variable points along the shaft as follows:

$$f_x^l(s) \approx \sum_{k=1}^N c_{xk} \delta(s - \sigma_k)$$

$$f_y^l(s) \approx \sum_{k=1}^N c_{yk} \delta(s - \sigma_k)$$
(8)

where $\delta(\cdot)$ is the Dirac delta function, c_{xk} and c_{yk} are magnitudes of the k^{th} point force in the local x and y directions, and σ_k is the arc length location of the k^{th} force. To implement this force distribution in the Cosserat model, we apply a step change to the internal force at each σ_k as follows:

$$\mathbf{n}(\sigma_k^+) = \mathbf{n}(\sigma_k^-) - \mathbf{R}(\sigma_k) \begin{bmatrix} c_{xk} \\ c_{yk} \\ 0 \end{bmatrix}$$

Note that the force locations σ_k can vary in this representation. We allow them to "slide" to arbitrary locations along the rod by parameterizing them within the unknown parameter vector \mathbf{x} to be optimized, along with the coefficients c_{xk} and c_{yk} . To keep the force application points σ_k on the interval $\begin{bmatrix} 0 & L \end{bmatrix}$ we define each one in terms of a parameter β_k as follows

$$\sigma_k = \frac{L}{2} + \frac{L}{2}\sin\beta_k$$

Thus, the sliding Dirac delta representation is able to exactly capture the effect of N point loads at N arbitrary points using a total of 3N variables.

To summarize, in the case of the Fourier series representation, the full unknown parameter vector in (1) has the following form:

$$\mathbf{x} = \begin{bmatrix} \mathbf{p}_0^\top & \boldsymbol{\theta}_0^\top & \mathbf{n}_0^\top & \mathbf{m}_0^\top & \boldsymbol{\alpha}^\top & \mathbf{a}^\top & \mathbf{b}^\top \end{bmatrix}^\top \tag{9}$$

where $\boldsymbol{\theta}_0 = [\theta_x \ \theta_y \ \theta_z]^{\top}$ contains Euler angles which define the base orientation \mathbf{R}_0 , $\boldsymbol{\alpha} = [\alpha_1 \cdots \alpha_{N_p}]^{\top}$ contains the parameters that define the comparison arc lengths, $\mathbf{a} = [a_{x0} \cdots a_{xk} \cdots a_{y0} \cdots a_{yk}]^{\top}$ and $\mathbf{b} = [b_{x1} \cdots b_{xk} \cdots b_{y1} \cdots b_{yk}]^{\top}$. In the case of the sliding Dirac delta representation, \mathbf{x} is

$$\mathbf{x} = \begin{bmatrix} \mathbf{p}_0^{\mathsf{T}} & \boldsymbol{\theta}_0^{\mathsf{T}} & \mathbf{n}_0^{\mathsf{T}} & \mathbf{m}_0^{\mathsf{T}} & \boldsymbol{\alpha}^{\mathsf{T}} & \mathbf{c}^{\mathsf{T}} & \boldsymbol{\beta}^{\mathsf{T}} \end{bmatrix}^{\mathsf{T}}$$
(10)

where
$$\mathbf{c} = [c_{x1} \cdots c_{xk} \cdots c_{y1} \cdots c_{yk}]^{\top}$$
 and $\boldsymbol{\beta} = [\beta_1 \cdots \beta_k]^{\top}$.

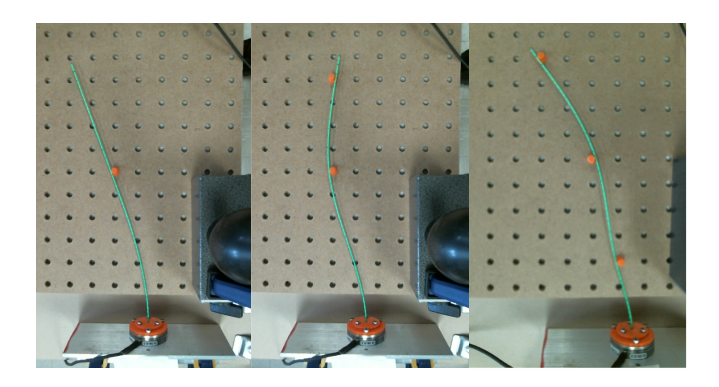


Fig. 3. The experimental setup consisted of a painted green rod, an ATI 6-DoF force/torque sensor, a mounted camera, and pegboard. The images shown above were used by the sensing algorithms for the single load test 14 (in Table II), the double load test 6 (in Table II), and a three load test.

D. Dealing with Ill Conditioning

Initial simulation results on simple beam problems revealed that a variety of different force distributions can approximate the same discrete shape dataset with near-zero shape error. This is the classic ill-conditioning issue that is typical of such "inverse problems" across many fields, as reviewed in [24]. However, identifying a possible force distribution that minimizes shape error is still potentially useful: the basic shape of the distribution as well as regions of high interaction force can be identified. We would also like to identify, in some sense, the "worst-case" force distribution. Among all distributions that fit the data well, we could postulate that the "worst-case" is the one in which the force is concentrated at the fewest locations. Based on this idea, we propose a simple sequential optimization procedure to estimate the "worstcase" force distribution. We solve a series of optimization problems where the distributed force is represented by a collection of N point forces (8), incrementing N by one for every new problem. The first problem assumes only one point force (N=1), the second two (N=2), and so on. If a solution yields an RMS shape error less than a specified tolerance (the expected shape measurement error), we use the current estimated force distribution without exploring larger numbers of point forces. Thus, we find the solution with the minimum number of point forces which also minimizes the objective function within a predefined tolerance. This may be a good proxy for the "worst-case" force distribution, and the estimated contact force magnitudes could be used for user feedback.

III. EXPERIMENTAL VALIDATION

To test our proposed force sensing framework we performed a series of experiments which compare the performance of the Fourier series representation with the set of point loads representation. We consider planar experimental cases, but the full 3D Cosserat model and optimization framework is used to fit the planar data. The experimental conditions included a set of 18 cases where a single point force was applied at various

unknown locations along a rod and a set of 6 cases where two point forces were applied at various unknown locations. An appropriate number of terms for the Fourier series (for adequate resolution of point loads without over-fitting) was determined to be 21 using two cases from the data set. The number of discrete terms used in the point load method was determined during the optimization using the iterative process detailed in the previous section. Point loads are the most difficult cases for the Fourier series to approximate. In contrast, the sliding Dirac deltas should be able to determine the appropriate number of forces and represent these cases exactly. We will see that both methods perform well in terms of attaining near-zero shape error and determining the location of high-force regions and load magnitudes.

A. Experimental Setup and Data Capture

The setup, shown in Figure 3, consisted of an elastic metal rod, a pegboard, an ATI 6-DoF force/torque sensor Nano 43 SI-36-0.5 (used only for validation), and an HD 1920x1080 Logitech digital camera held by a Noga Articulated Holder MG71003. We performed experiments on two different rods (of lengths 0.2 m and 0.3 m), both with a diameter of 1.4 mm ($I = J/2 = 1.89 \times 10^{-13} m^4$) and made from ASTM A228 spring steel, which has a Young's modulus of 207 GPa and shear modulus of 79 GPa. The rods were painted green for enhanced visibility, mounted to the force sensor, and subjected to point loads by small plastic cylinders.

In each experiment, a set of discrete shape data points \mathbf{d}_i is obtained by processing a single camera image (shown in figure 4). We used color thresholding to isolate the pixels that correspond to the rod shape and obtain an ordered list of shape data points and arc lengths by employing a sliding window of pixels starting at the base of the rod and iteratively propagating the window forward along the approximate tangent vector. At each step we calculate the centroid of the rod pixels within the current window and then slide the window by a fixed distance in the the direction of the centroid until the end of the rod is reached. For the 30 cm and 20 cm rod experiments, $N_p=134$ and $N_p=98$.

B. Procedure

In the first set of experiments, a single peg was used to create loading conditions at varying contact locations along each rod, which are listed in Table I, some of which are shown in the top row of Figure 4. In a second set of experiments, we used two pegs to deform the rods by applying a set of two loads at various locations. 3 different loading conditions were analyzed for each rod, which are listed in Table II. The three two-peg experiments for the 30 cm rod are shown in the second row of Figure 4.

To measure the ground-truth arc-length location of the applied forces, the undeformed rod was marked with ticks, 1mm apart, using a ruler, and the locations were identified manually. In the single-load experiments we obtained the ground-truth applied force vector directly from the base mounted force sensor (since for a single peg, the measured

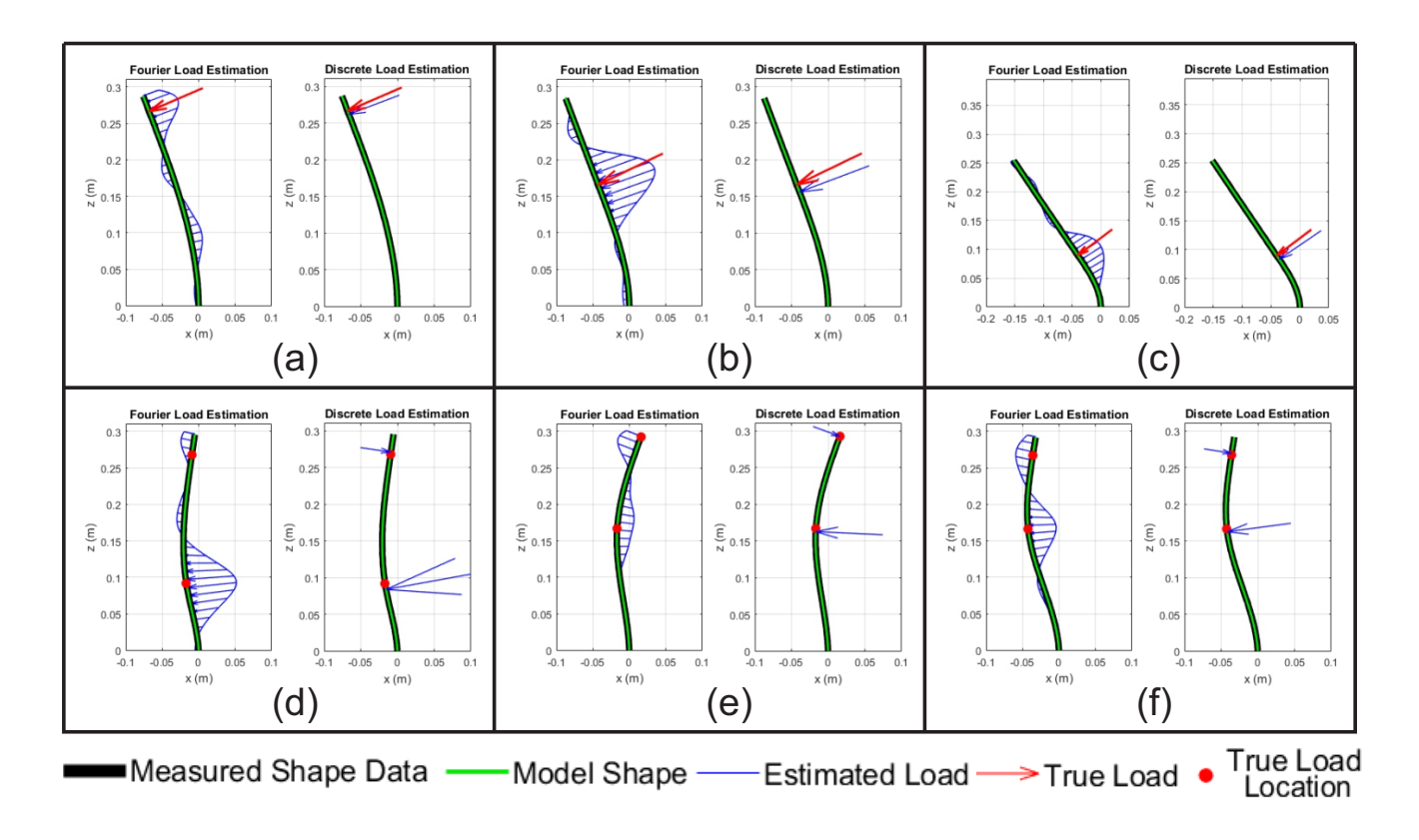


Fig. 4. A subset of our experimental results is shown in the plots above, comparing the performance of our optimization approach with the two different force representations. In the single force cases on the top row, the estimated loads are compared to the ground truth load as measured by the base mounted sensor. Sub-figures (a), (b), and (c) correspond to tests 18, 14, and 12 in Table I. On the second row, the ground-truth force locations are compared to the estimated loadings. Note that the magnitudes of the distributed forces and point forces on the plot should not be directly compared since they have different physical units and are scaled by different arbitrary amounts for visibility. Sub-figures (d), (e), and (f) correspond to tests 4, 5, and 6 in Table II.

base force should equal the applied force from the peg). The sensor is used only for validation and does not provide any information to the estimation algorithms. In the two-load case, the individual ground-truth loads are not directly measurable using only the base measured force, but we can still compare the measured force at the base to the resultant of the estimated force distribution, computed by integrating it over the entire length (where the integral of a Dirac delta function is 1 by definition, so integrating merely sums up the discrete loads).

C. Results

For the point-force representation, the ground-truth force vector and location can be directly compared to the estimated ones, as shown in Figure 4. For the Fourier series representation, we compare the ground-truth load location to the location of the highest peak on the force distribution, and we compare the ground-truth load magnitude to the integral of the Fourier force distribution over the length. Note that the size of the distributed forces and point forces shown in Figure 4 should not be directly compared since they have different units and are scaled by different amounts for visibility.

Table I lists the RMS shape error of both methods, the arc-length location, and the load magnitude for all the single

 $\label{eq:table_interpolation} TABLE\ I$ Summary of Single Load Experimental Results

Rod Length	Test Number	RMS Shape Error (mm)		Arc L	ength Loc (mm)		Magnitude (N)			
Length	Number	Fourier Series	Sliding Dirac Delta	Ground Truth	Fourier Series	Sliding Dirac Delta	Ground Truth	Fourier Series	Sliding Dirac Delta	
200 mm	1	0.085	0.086	67	62	65	4.17	5.44	4.44	
	2	0.067	0.067	92	84	90	1.71	2.10	1.82	
	3	0.093	0.091	99	90	94	4.29	5.39	4.60	
	4	0.071	0.069	117	123	115	0.89	0.98	0.93	
	5	0.079	0.075	123	127	118	2.32	2.46	2.38	
	6	0.099	0.097	133	134	130	3.15	3.17	3.12	
	7	0.082	0.079	167	179	159	0.32	0.36	0.36	
	8	0.063	0.066	171	165	165	0.88	1.00	0.89	
	9	0.086	0.082	180	186	177	1.34	1.13	1.26	
300 mm	10	0.075	0.068	68	66	64	4.96	5.06	4.52	
	11	0.124	0.076	93	91	83	2.24	2.52	2.74	
	12	0.151	0.136	100	93	93	4.43	5.71	5.17	
	13	0.130	0.078	169	161	156	0.40	0.46	0.45	
	14	0.112	0.069	173	167	163	0.99	0.96	1.02	
	15	0.148	0.118	182	185	179	1.35	1.28	1.29	
	16	0.166	0.111	270	279	264	0.11	0.14	0.10	
	17	0.125	0.082	272	258	270	0.27	0.19	0.24	
	18	0.127	0.086	278	277	273	0.40	0.49	0.37	

TABLE II SUMMARY OF DOUBLE LOAD EXPERIMENTAL RESULTS

Rod	Test	RMS Shape Error (mm)		Arc I	Length Loca (mm, mm)		Base Force Magnitude (N)		
Length	Number	Fourier Series	Sliding Dirac Deltas	Ground Truth	Fourier Series	Sliding Dirac Deltas	Ground Truth	Fourier Series	Sliding Dirac Deltas
200 mm	1	0.157	0.073	67, 194	72, 175	62, 198	8.60	7.87	9.61
	2	0.206	0.072	92, 168	87, 178	92, 166	5.16	6.10	5.18
	3	0.100	0.248	108, 193	125, 190	117, 197	3.62	3.18	3.53
300 mm	4	0.187	0.087	94, 272	90, 289	87, 276	4.01	4.18	4.48
	5	0.147	0.084	169, 300	179, 284	166, 300	1.89	2.21	1.85
	6	0.141	0.084	173, 275	175, 273	171, 277	2.67	2.21	2.58

force cases, comparing estimated values to the true applied values in each case. Over the 18 single load cases, the average error in load location was 6 mm (2-3% of total rod length) for the Fourier series approximation and 5 mm for the Dirac delta approximation. The average error in load magnitude was 0.30 N and 0.16 N, respectively. The 6 two loads cases are listed in Table II. The average error in load location was 9 mm for the Fourier series and 4 mm for the for the Dirac delta. The average base force magnitude error was 0.51 N and 0.29 N, respectively.

The results indicate that the Dirac delta approximation provided an overall more accurate representation of the loads. This was expected as the Fourier series is fundamentally limited when describing point loads. We chose this set of experiments because we believe that the most important application of the distributed force estimation problem is to identify the locations and magnitudes of highly concentrated forces. Since this is also the most difficult case for the Fourier series to represent, these experiments are a good stress test for finding the limits of its ability.

D. Further Examples: Complex and 3D Load Cases

In addition to our main experimental dataset, we further demonstrate the generality of the approach by including two ad hoc experimental examples of more complex cases. First, Figure 5 shows an experiment with 3 point loads that create multiple inflection points. The results are consistent with our main dataset indicating that more complex loadings can be handled. Second, we show the results from a much more challenging 3D loading experiment in Figure 6. We used a 3D printed rod with a 4mm square cross section made of thermoplastic polyurethane. To achieve a 3D, nonplanar deformed shape, the rod was printed into a precurved "U" shape, and gravity was used to apply an out of plane distributed load. In this large-deflection scenario, torsion is a significant contributor to the deformed shape. We used orthogonal camera views to determine the 3D shape, and applied our Fourier estimation method with N=21 terms. Despite the fact that a global gravity load violates our modeling assumption that the loading is orthogonal to the rod tangent vector, the results shown in Figure 6 display an estimated load of approximately the right magnitude and direction. The RMS shape error over the length is 2.64 mm (whereas the width of the rod is 4 mm, and the total length is 190 mm). This example indicates that the inverse problem

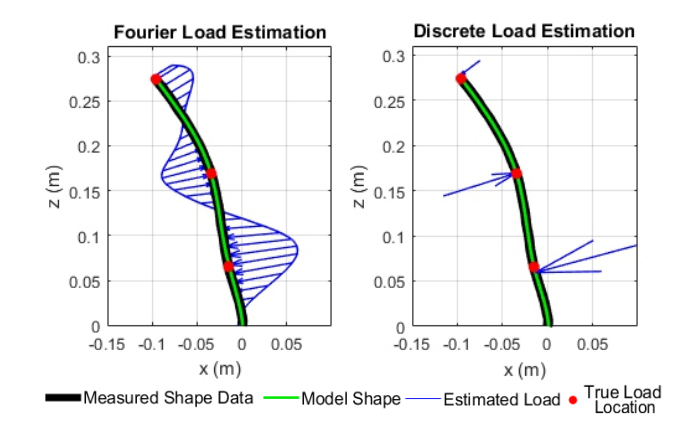


Fig. 5. We include this additional ad hoc example of a three-load case to further demonstrate the generality of the approach. Even with alternating curvatures, both distributed load approximations are capable of achieving near-zero shape error, and the estimated distributions have peaks near the true contact points.

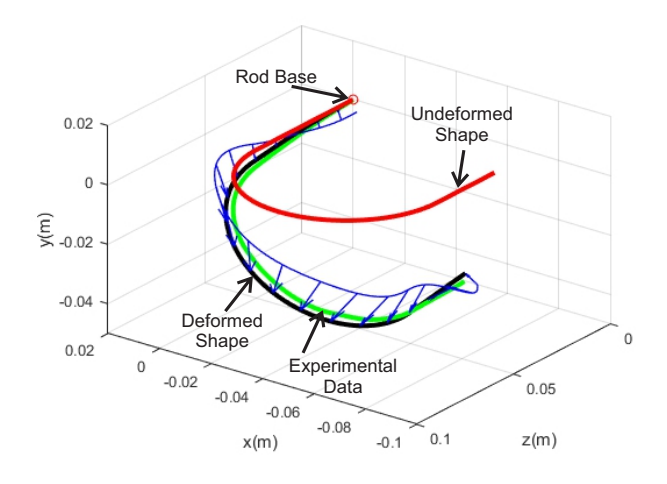


Fig. 6. In theory, the algorithms presented are capable of force estimation for 3D rod shapes and distributed loading. Here we present a test example where a soft "U" shaped rod structure is deformed by gravity.

is perhaps more ill-conditioned in 3D cases with significant torsion, but the method still gives useful information about loading conditions consistent with the observed shape.

IV. CONCLUSIONS

Our conclusion from these studies is that even though the distributed force estimation problem is an ill-posed inverse problem, approaching it from a constrained optimization perspective has the potential to yield useful information about the location and magnitudes of forces on soft/continuum robots and flexible devices. Experimental results on a single large-deflection rod showed that image-based shape data can be matched extremely well by a Cosserat model with various force distributions that corresponded in certain respects to the true force distribution on the rod. In future work, we aim to adapt this approach and increase its speed in order to estimate forces on actuated soft/continuum robots in real-time for operator feedback and/or force control.

REFERENCES

- M. Mahvash and P. E. Dupont, "Stiffness Control of Surgical Continuum Manipulators.," *IEEE Transactions on Robotics*, vol. 27, pp. 334–345, apr 2011.
- [2] D. C. Rucker and R. J. Webster III, "Deflection-Based Force Sensing for Continuum Robots: A Probabilistic Approach," *IEEE/RSJ International Conference on Intelligent Robots and Systems*, pp. 3764–3769, 2011.
- [3] M. Khoshnam, A. C. Skanes, and R. V. Patel, "Modeling and Estimation of Tip Contact Force for Steerable Ablation Catheters," *IEEE Transactions on Biomedical Engineering*, vol. 62, pp. 1404– 1415, 5 2015.
- [4] A. Borum, D. Matthews, and T. Bretl, "State estimation and tracking of deforming planar elastic rods," in 2014 IEEE International Conference on Robotics and Automation (ICRA), pp. 4127–4132, IEEE, 5 2014.
- [5] S. Song, Z. Li, H. Yu, and H. Ren, "Shape reconstruction for wire-driven flexible robots based on Bézier curve and electromagnetic positioning," *Mechatronics*, vol. 29, pp. 28–35, 8 2015.
- [6] H. Yuan, P. W. Y. Chiu, and Z. Li, "Shape-Reconstruction-Based Force Sensing Method for Continuum Surgical Robots With Large Deformation," *IEEE Robotics and Automation Letters*, vol. 2, pp. 1972– 1979, 10 2017.
- [7] R. Xu, A. Yurkewich, and R. V. Patel, "Curvature, Torsion, and Force Sensing in Continuum Robots Using Helically Wrapped FBG Sensors," *IEEE Robotics and Automation Letters*, vol. 1, pp. 1052–1059, 7 2016.
- [8] F. Khan, R. J. Roesthuis, and S. Misra, "Force sensing in continuum manipulators using fiber Bragg grating sensors," in 2017 IEEE/RSJ International Conference on Intelligent Robots and Systems (IROS), pp. 2531–2536, IEEE, 9 2017.
- [9] K. Xu and N. Simaan, "Intrinsic Wrench Estimation and Its Performance Index for Multisegment Continuum Robots," *IEEE Transactions on Robotics*, vol. 26, no. 3, pp. 555–561, 2010.
- [10] C. B. Black, J. Till, and D. C. Rucker, "Parallel Continuum Robots: Modeling, Analysis, and Actuation-Based Force Sensing," *IEEE Transactions on Robotics*, vol. 34, pp. 29–47, 2 2018.
- [11] T. W. Bretl and Z. McCarthy, "Quasi-Static Manipulation of a Kirchhoff Elastic Rod based on a Geometric Analysis of Equilibrium Configurations," *The International Journal of Robotics Research*, vol. 33, no. 1, pp. 48–68, 2014.
- [12] S. Hasanzadeh and F. Janabi-Sharifi, "Model-based Force Estimation for Intra-cardiac Catheters," *IEEE/ASME Transactions on Mechatronics*, vol. 21, no. 1, pp. 1–1, 2015.
- [13] J. Back, L. Lindenroth, R. Karim, K. Althoefer, K. Rhode, and H. Liu, "New kinematic multi-section model for catheter contact force estimation and steering," in 2016 IEEE/RSJ International Conference on Intelligent Robots and Systems (IROS), pp. 2122–2127, IEEE, 10 2016.
- [14] A. Bajo and N. Simaan, "Finding lost wrenches: Using continuum robots for contact detection and estimation of contact location," in 2010 IEEE International Conference on Robotics and Automation, pp. 3666–3673, IEEE, 5 2010.
- [15] A. Bajo and N. Simaan, "Kinematics-Based Detection and Localization of Contacts Along Multisegment Continuum Robots," *IEEE Transac*tions on Robotics, vol. 28, pp. 291–302, 4 2012.
- [16] E. Coevoet, A. Escande, and C. Duriez, "Optimization-Based Inverse Model of Soft Robots With Contact Handling," *IEEE Robotics and Automation Letters*, vol. 2, pp. 1413–1419, 7 2017.
- [17] P. L. Anderson, A. W. Mahoney, and R. J. Webster, "Continuum Reconfigurable Parallel Robots for Surgery: Shape Sensing and State Estimation With Uncertainty," *IEEE Robotics and Automation Letters*, vol. 2, no. 3, 2017.
- [18] Z. Zhang, J. Dequidt, and C. Duriez, "Vision-Based Sensing of External Forces Acting on Soft Robots Using Finite Element Method," *IEEE Robotics and Automation Letters*, vol. 2018, no. 3.
- [19] D. C. Rucker, B. A. Jones, and R. J. Webster III, "A Geometrically Exact Model for Externally Loaded Concentric-Tube Continuum Robots," *IEEE Transactions on Robotics*, vol. 26, pp. 769–780, 10 2010.
- [20] D. C. Rucker and R. J. Webster III, "Statics and Dynamics of Continuum Robots With General Tendon Routing and External Loading," *IEEE Transactions on Robotics*, vol. 27, pp. 1033–1044, 12 2011.
- [21] J. Till, C. E. Bryson, S. Chung, A. Orekhov, and D. C. Rucker, "Efficient computation of multiple coupled Cosserat rod models for real-time simulation and control of parallel continuum manipulators," in 2015 IEEE International Conference on Robotics and Automation (ICRA), pp. 5067–5074, IEEE, 5 2015.

- [22] D. C. Rucker and R. J. Webster III, "Computing jacobians and compliance matrices for externally loaded continuum robots," *IEEE International Conference on Robotics and Automation*, 2011.
- [23] R. M. Murray, Z. Li, and S. Sastry, A mathematical introduction to robotic manipulation. CRC Press, 1994.
- 24] S. I. Kabanikhin, "Definitions and examples of inverse and ill-posed problems Survey paper," *J. Inv. Ill-Posed Problems*, vol. 16, pp. 317– 357, 2008.